BBA - Molecular and Cell Biology of Lipids 1870 (2025) 159568

Contents lists available at ScienceDirect

BBA - Molecular and Cell Biology of Lipids

journal homepage: www.elsevier.com/locate/bbalip

Lipid imaging mass spectrometry: Towards a new molecular histology

Ibai Calvo [a], Olatz Fresnedo [b], Lorena Mosteiro [c], José I. López [d], Gorka Larrinaga [d,e,f,*], José A. Fernández [a,**]

[a] Department of Physical Chemistry, Faculty of Science and Technology, University of the Basque Country (UPV/EHU), Barrio Sarriena S/N, 48940 Leioa, Spain
[b] Lipids&Liver, Department of Physiology, Faculty of Medicine and Nursing, University of the Basque Country (UPV/EHU), B. Sarriena, s/n, Leioa 48940, Spain
[c] Department of Pathology, Cruces University Hospital, 48903 Barakaldo, Spain
[d] Biobizkaia Health Research Institute, 48903 Barakaldo, Spain
[e] Department of Nursing, Faculty of Medicine and Nursing, University of the Basque Country (UPV/EHU), B. Sarriena, s/n, Leioa 48940, Spain
[f] Department of Physiology, Faculty of Medicine and Nursing, University of the Basque Country (UPV/EHU), B. Sarriena, s/n, Leioa 48940, Spain

ARTICLE INFO

Keywords:
MALDI-imaging
Lipidomics
Molecular histology
Renal cell carcinoma
cancer
Digital histopathology

ABSTRACT

Lipid research is attracting greater attention, as these molecules are key components to understand cell metabolism and the connection between genotype and phenotype. The study of lipids has also been fueled by the development of new and powerful technologies, able to identify an increasing number of species in a single run and at decreasing concentrations. One of such key developments has been the image techniques that enable the visualization of lipid distribution over a tissue with cell resolution. Thanks to the spatial information reported by such techniques, it is possible to associate a lipidome trait to individual cells, in fixed metabolic stages, which greatly facilitates understanding the metabolic changes associated to diverse pathological conditions, such as cancer. Furthermore, the image of lipids is becoming a kind of new molecular histology that has great chances to make an impact in the diagnostic units of the hospitals. Here, we examine the current state of the technology and analyze what the next steps to bring it into the diagnosis units should be. To illustrate the potential and challenges of this technology, we present a case study on clear cell renal cell carcinoma, a good model for analyzing malignant tumors due to their significant cellular and molecular heterogeneity.

1. Introduction

The study of lipids is a complex subject, due to the enormous number of species present in a cell at a given metabolic stage, with very similar structure or even with the same atomic composition [1]. Let us take, for example, the case of glycerophospholipids (GPLs): identifying a molecular species involves determining the nature of the polar head, the length of the fatty acids, the number of insaturations, their position and their cis or trans conformation. All these aspects may be relevant to understand the role that each lipid species plays in the metabolism of a cell [2]. To add to this complexity, the same lipid species may not play the same role in two different cells [3]. Furthermore, lipid composition is dynamic and continuously changing and remodeling in response to the metabolic stage and cell's requirements [4]. What is more amazing, this adaptive process is strictly regulated to the point of presenting an impressive reproducibility among individuals [5,6].

Therefore, it is of no surprise that analyzing the lipidome of a given tissue is a methodological challenge. The development of analytical techniques based on mass spectrometry (MS) has helped to solve, at least partially, this problem [7]. MS comprises a number of techniques that aim at determining the identity of the molecular species in a sample, based on their molecular weight. In its most popular variant, mass spectrometers are usually coupled to a previous high-performance liquid chromatography stage, or HPLC. This HPLC-MS combination constitutes a powerful analytical tool, able to identify hundreds or even thousands of species in a single run [8]. Thus, it is the technique of choice for the analysis of lipids in biological samples: from body fluids to tissue homogenates.

The second most popular technique to introduce samples into a mass spectrometer is matrix-assisted laser desorption/ionization (MALDI) [9–11]. It is specially designed to analyze solid samples and it is based in Tanaka's developments around the transfer of thermolabile samples into gas phase [10]. However, it lacks the separation stage present in HPLC-MS and therefore, its analytical power is significantly reduced. On the

* Corresponding author at: Biobizkaia Health Research Institute, 48903 Barakaldo, Spain.
** Corresponding author.
E-mail addresses: gorka.larrinaga@ehu.eus (G. Larrinaga), josea.fernandez@ehu.eus (J.A. Fernández).

https://doi.org/10.1016/j.bbalip.2024.159568
Received 19 July 2024; Received in revised form 25 September 2024; Accepted 3 October 2024
Available online 5 October 2024

other hand, it was the basis for the development of MALDI-imaging mass spectrometry (MALDI-IMS) in the '90s [12,13]. Such technical evolution has enabled, for the first time, to add spatial information to the molecular analysis of biological samples. The analysis (Fig. 1) starts with a sample that has been extracted and frozen in liquid nitrogen, avoiding as much as possible the use of chemical substances (cryoprotectant compounds, fixation, optimal cutting temperature compounds –OCT– etc.). Then, 6–20 μm-thick sections are obtained with the aid of a microtome-cryostat and deposited in either plain or ITO-covered (indium-tin oxide-covered) microscope slides. Next step is critical: the sample has to be uniformly covered with an organic substance, the matrix, which will help extracting the analytes with the aid of a laser in the MALDI source of the mass spectrometer. Exploration of the sample is done following a pre-defined array of coordinates that will become the pixels in the final image. Separation between coordinates will determine the maximum spatial resolution of the images, which typical goes from 100 to 10 μm/pixel, although smaller pixel sizes have been occasionally reported [14].

Once the image is acquired, it is possible to reconstruct the distribution of each of the ions detected by representing the integral of each mass channel against the acquisition coordinates. Data analysis is usually done in two ways: examining the individual lipid distribution images and using segmentation algorithms that permit associating a lipid signature to specific histological structures, cell populations or even subpopulations.

Identification of lipids directly from the tissue is not an easy task, and usually requires of combination with data previously obtained using LC-MS/MS. It is possible to run MS/MS experiments directly on the tissue, but it is a cumbersome task hampered by ion suppression effects. The incorporation in the mass spectrometers of improved ion mobility sources may help improving direct lipid identification in LIMS experiments.

That was the "traditional" protocol for a standard MALDI-IMS experiment and, in general, for other variants that are becoming increasingly popular like DESI-IMS (desorption electro-spray ionization-IMS) [15] or LAESI-IMS (laser ablation electrospray ionization-IMS) [16]. Such variants differ in the method used for scanning the sample and introducing the analytes into the mass spectrometer, but they share the rest of the protocol. Therefore, in the following we will refer to all of them as lipid imaging mass spectrometry (LIMS).The enormous amount of information generated at each LIMS experiment and the absence of previous information on the lipid composition of the tissues, has highlighted the necessity of going one-step beyond this "traditional" methodology, if one wants to extract the most out of an experiment.

The most evident way to understand LIMS images is by direct comparison with a post-MALDI stained image. If sample exploration is carried out correctly, the tissue suffers very little damage and, after matrix removal using an acetone/methanol solution, it can be properly stained for histological analysis and annotation by a pathologist under the microscope. For example, Fig. 2B (and S1 of the supplemental material) shows the microscopic image of a human kidney section, corresponding to the transition zone between cortex and medulla, stained with hematoxylin-eosin (H&E). Four glomeruli are readily seen in the upper-left half of the image and an artery in the lower-right corner. The remaining structures in the picture are proximal and distal tubules and collecting ducts. It is very difficult for a pathologist to go any further on the analysis of that image.

Fig. 2C–G shows the segmentation analysis of the LIMS experiment carried out over the section in Fig. 2B. The image can be arbitrarily divided into a number of segments to extract the lipid fingerprints corresponding to the different cell populations. Thus, as the number of segments increases, the tissue histology becomes clearer: glomeruli and interstitial tissue are grouped in a segment, while different types of tubules show up. However, there is always a risk of over-interpreting the experimental results. There is an extensive literature regarding image

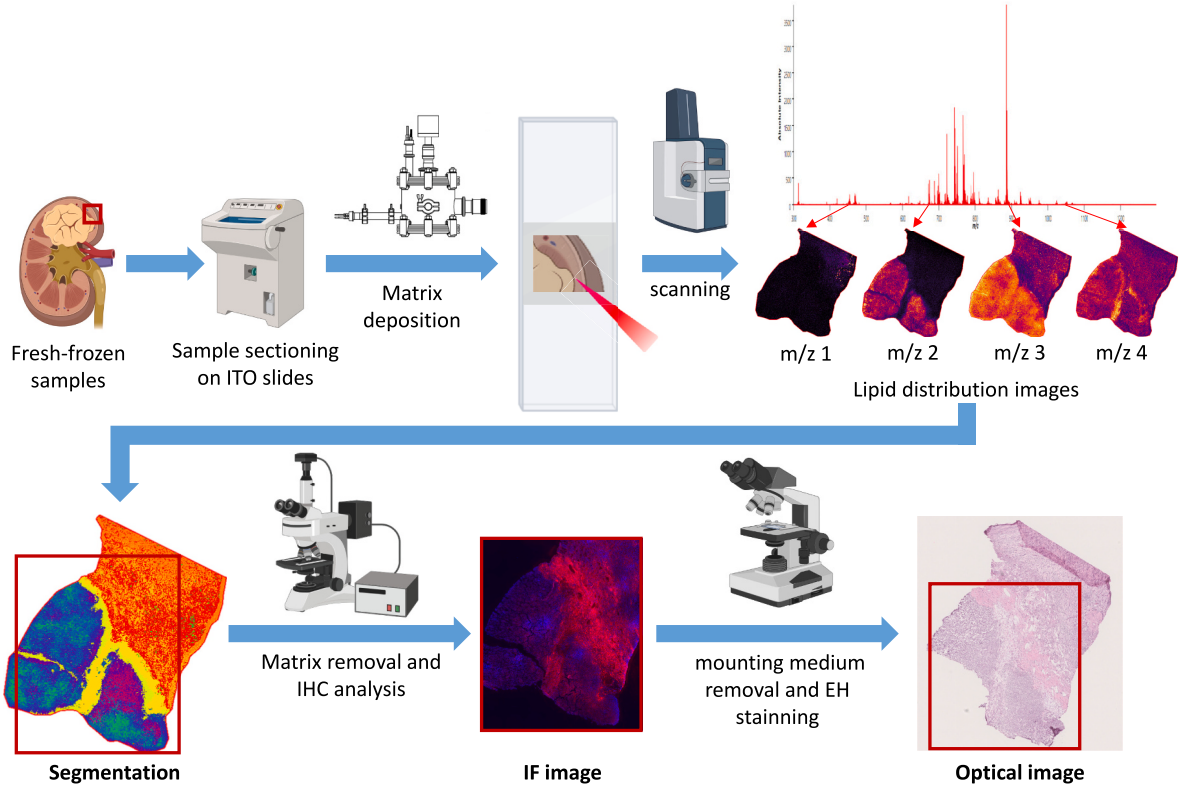

Fig. 1. Workflow of a typical MALDI-imaging experiment. Samples are collected and immediately frozen. Then 6–20 μm-thick sections are obtained with the aid of a cryo-microtome and deposited in glass slides. The sample is covered with matrix and introduced into a mass spectrometer, where it is scanned. Using specialized software, the distribution of each of the m/z channels in the spectrum is reconstructed, together with the segmentation image. Then, the matrix is removed and the tissue is incubated with different fluorescence-labelled antibodies. In the best cases, the mounting medium can also be removed and perform a final H&E staining.

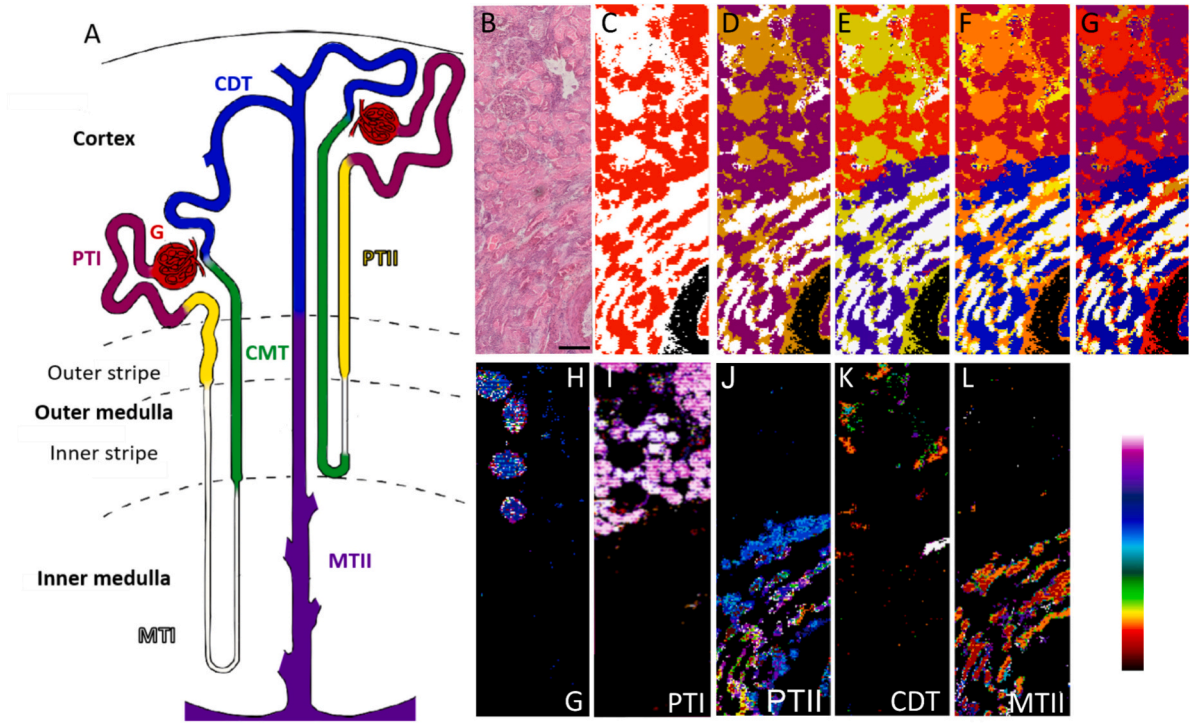

Fig. 2. LIMS offers a kind of new histology. A) Sketch of a nephron with the segments identified by LIMS highlighted; B) optical image of an H&E staining of a corticomedullary section of healthy human kidney; (C)–(G) segmentation images of a LIMS experiment performed over the same section, with the image divided into 2, 3, 4, 6 and 20 segments, respectively, based on the similarity of the lipid fingerprint at each pixel; (H)–(L) segments corresponding to glomeruli (G), type I and II proximal tubules (PT I and II), cortical distal tubules (CDT) and type II medullary tubules (MT II) that were segregated and re-analyzed, showing further heterogeneity in the lipid fingerprint. Experiment carried out in negative polarity at 10 μm/pixel of spatial resolution. The segments were colored using the scale bar in the figure the correlation, so the segments that exhibit a more similar lipid fingerprint show colors that are closer in the scale. Adapted from Ref [17]. See also Fig. S1 of the supplemental information.

segmentation in LIMS [18–21], which remarks that the problem is still not solved. Probably the most commonly used algorithm for segmentation is k-means. It has proven to offer an acceptable ability to identify the most relevant features in a LIMS experiment. However, it may lead to different results in consecutive runs over the same sample, because k-means choses the initial points randomly. An alternative approach consists of letting the user to guide the segmentation process, like in SILCS software (Bruker Daltonics Inc.), but this procedure, although enables solving certain problems encountered during the segmentation process, is highly subjective and may lead to creating artificial divisions of the images. Certainly, only by comparison with, for example, standard immunohistochemistry (IHC) images, it is possible to determine the optimal number of segments in which the experiment can be divided. Using such methodology, LIMS experiment followed by IHC (or immunofluorescence, IF) over the same tissue section, Martín-Saiz et al. [17] were able to identify eight different histologic areas in human kidney, each of them with its own lipid signature. Such signature is maintained among individuals, as demonstrated in the same work. However, it is difficult to really extract all the information from a LIMS experiment carried out with cell resolution. Very often, part of the information still remains hidden in the LIMS images. At some point, it is necessary to isolate the segments, segregate them and re-analyze to capture all the lipid heterogeneity (Fig. 2H–L). It is becoming commonly accepted that the LIMS segmentation images are able to highlight the existence of every single cell population, with a precision far beyond that of the traditional histology [22–25].

Thus, it is becoming more common to complement MALDI-IMS experiments with additional IHC, IF or other techniques that facilitate understanding of lipid distribution images [8,17,25–28]. Such experiments should be preferably performed in the same section scanned by MALDI-IMS, especially if the experiment was recorded at high spatial resolution, or if the section corresponds to a complex sample, such as a tumor. Otherwise, the overlapping between optical and IMS images becomes complicated.

The high level of reproducibility of the lipid fingerprint of a cell population obtained by this methodology and its exquisite sensitivity to detect early alterations make LIMS a potential candidate for defining a new molecular histology, which would enable the analysis of tissues based on their molecular composition. This is by no means an easy task: it has been demonstrated that the lipid composition of a given cell is preserved among individuals, but it is necessary to associate each cell type phenotype with its lipidome. This task alone will require of an overwhelming number of experiments. But, in addition, it will be necessary to identify the changes that each pathology produces in the lipidome of the cells.

A step forward in this context would be the application of this methodology to cancer samples, to know more about its diverse pathophysiology, again, associating specific lipidomic signatures with 2022 WHO-recognized tumor subtypes [29]. As an example, we will show below some cases in which LIMS experiments enable visualization of clear cell renal cell carcinoma (ccRCC) tumors in transition samples, yielding important information, difficult to capture by other traditional techniques. ccRCC is a common and aggressive histological variant of renal cancer in Western countries. The molecular hallmark of ccRCC is the malfunction of the von Hippel-Lindau (VHL) gene, which is located in the short arm of chromosome 3. This genetic defect has been extensively studied and, in brief, induces a false status of intracellular hypoxia, which in turn develops a pro-angiogenic environment via the hypoxia-inducible factor (HIF)-vascular endothelial growth factor Receptor (VGFR) cascade [30]. In fact, ccRCC is a paradigmatic example of tumor neo-angiogenesis [29,30]. Despite extensively studied due to its important impact in the public health systems worldwide, the exact cell

population from which this tumor originates remains under debate. The most accepted theory indicates that it originates in the epithelial cells of the proximal tubule of the nephron [31,32], although other alternatives have also been proposed [33]. Since LIMS defines a specific lipidomic fingerprint in every part of the nephron, this methodology may clarify this debated issue if the lipidic signatures of the epithelial cell in the proximal tubule are identified. In the following, we present several examples of experiments carried out over ccRCC sections, which will serve us to demonstrate the potential of LIMS as a molecular histology technique.

2. LIMS images accurately describe the architecture of human kidney

Human kidney is a very well organized tissue. Its functional unit, the nephron, starts in the renal cortex. Histologically, the nephron begins with the glomerulus, a tuft of capillaries encased in Bowman's capsule, followed by the proximal tubule (Fig. 2A). It then continues through the Loop of Henle in the medulla, the distal convoluted tubule back in the cortex, and ends in the collecting duct [34]. Previous studies demonstrated that several segments can be identified, based on their lipid profile. Certainly, each cell type presents a characteristic lipid fingerprint. Therefore, as the cell composition of the nephron changes, it also does the lipid composition of each segment. In the study of Martín-Saiz et al. [17], we demonstrated that up to eight segments of the nephron could be identified based on their lipid fingerprint (Fig. 2A): the glomeruli, two segments of the proximal tubule (PT) called PT I and PT II corresponding to the cortical convoluted and the straight part of PTs, respectively; two medullary tubules called MT I and MT II and associated with the thin part of the loop of Henle and the medullary part of collecting ducts; corticomedullary tubules (CMT), which likely correspond to the thick ascending limb of the loop of Henle; corticodistal tubules (CDT), corresponding to the cortical portion of the distal nephron (distal tubules, connecting tubules and cortical collecting ducts); and interstitial structures.

Fig. 3 shows an example of how the lipid distribution images highlight the architecture of a human kidney section. The distribution of several lipids is shown, each of them presenting different relative abundances in the histological areas: while PE p40:6 (m/z = 774.541) is mostly localized in glomeruli and connective tissue, PE 34:2 (m/z = 714.506) highlights the position of the PTI. PE e38:5 (m/z = 750.542, Fig. 3D), delimits the MT II; SHexCer 42:1(2OH) (m/z = 906.631, Fig. 3E) is more abundant in CDT and CMT and SHexCer 42:1 (OH) (m/z = 1068.681, Fig. 3F) is more abundant in PTII. An enlarged version of the figure and detailed comparison with the histological section may be found in Figs. S2 and S3 of the Supplemental material.

The segmentation analysis (Fig. 3G) reproduces the rich architecture of the kidney, in which the different segments of the nephron have their own and characteristic lipid signature. Once more, it is difficult to achieve a complete segmentation of such a complex experiment, especially because it is not clear how many different lipid signatures the experiment contains. There is extensive literature dealing with the development of segmentation algorithms to analyze LIMS experiments [35–38] and the issue is far from being solved. Complete assignment of the lipid fingerprints would require of comparison with multiple IF experiments and in some cases, the required antibodies are not available. However, it is possible to identify those segments of the nephron already identified in previous works by comparison with the reported lipid signatures [17,39]. In this way, the identifiable segments were highlighted in Fig. S2 of the supplemental material, following the color scheme of the nephron in Fig. 2A. It is worthy to note that the results in Fig. 3 were obtained using a time-of-flight (TOF) instrument, while those

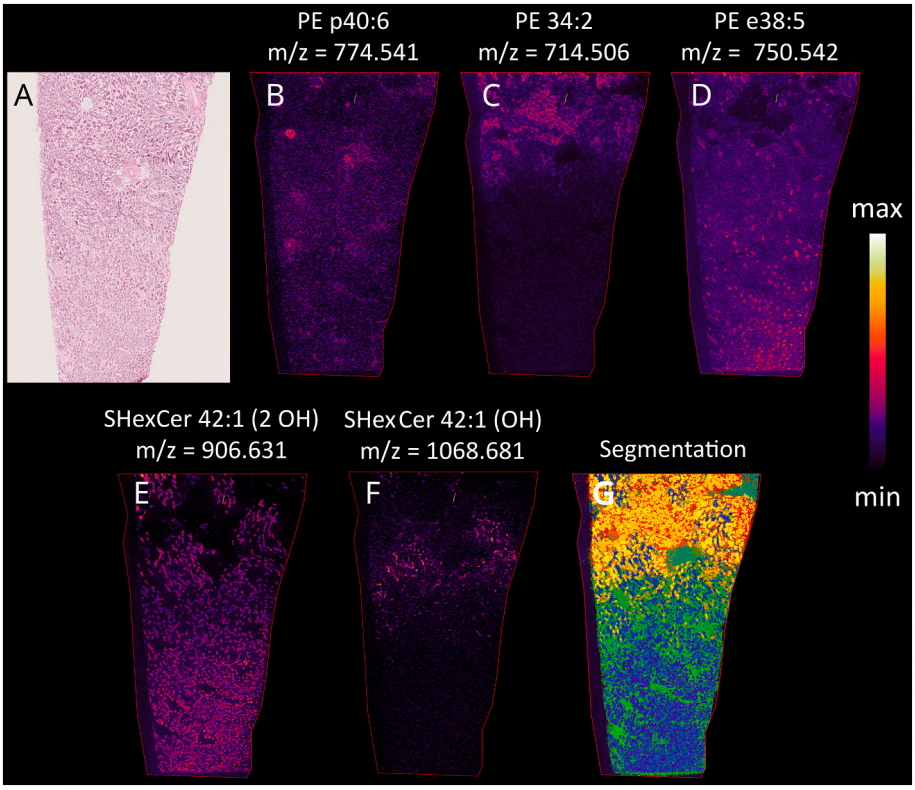

Fig. 3. A) H&E optical image of a human kidney section of the transition from cortex to medulla; (B)–(F) distribution of PE p40:6, PE 34:2, PE e38:5, SHexCer 42:1(2 OH) and SHexCer 42:1 (OH). Intensity follows the black-blue-orange-yellow-white scale bar in the figure; G) Segmentation analysis of the LIMS experiment. Segmentation was carried out in a supervised way, and the segments were identified by comparison with the lipid fingerprints in refs [17, 39]. Experiment carried out in negative polarity at 10 μm/pixel of spatial resolution. Scale bar 1 mm. See also supplemental Figs. S2 and S3. (For interpretation of the references to color in this figure legend, the reader is referred to the web version of this article.)

in ref. 17 were obtained with an orbitrap. Both the ion source and the technology behind the analyzer of both instruments are considerably different. Furthermore, while in reference 17 the segmentation analysis was carried out with an in-house designed, unsupervised segmentation algorithm, that in Fig. 3 was performed using commercial software and a supervised k-means algorithm. Still, the lipid signatures extracted with the later are very similar to those in ref. 17 to the point of being possible to associate them to the areas of the nephron previously mapped. This is an important observation as it confirms the reproducibility of the lipid fingerprint, not only among individuals, but also between different mass spectrometers.

The experiment in Fig. 3 contains approx. 300,000 pixels and covers a wide area of the kidney from the cortex to the inner medulla. Therefore, this is the first image in which all the segments obtained in our previous works coexist, enabling further confirmation of the identity of the segments simply by checking their relative position on the image.

3. Lipidomic connection between tumor cells and their parent cells

As stated in the introduction, LIMS does not require of any previous labelling. This characteristic confers the technique a great advantage respect other "traditional" techniques, which are limited to the availability of labelled molecules. This is especially true in the study of complex samples. Fig. 4 shows a transition between tumor and the uninvolved part of a kidney with ccRCC. The non-tumor kidney tissue, is mostly formed by cortical distal tubules (CDT), fibrotic tissue and glomeruli, the latter highlighted by the distribution of SM d34:1 (Fig. 4B). A small population of PT I may be found in the upper-left corner of the section. The presence of these tubules becomes evident in Fig. 4C, where the distribution of PC 36:4 is shown, which is more abundant in PT I. On the other hand, PI 36:4 (Fig. 4D) highlights the presence of CDT. Fig. 4E is a combination of SM d34:1 (red) and GM3 42:1 (green), demonstrating the high specificity of the lipid composition, which enables even distinguishing the Bowman's capsule of the glomeruli. The segmentation analysis also shows the presence of tumor tissue (Fig. 4F, bright green and purple). Actually, just by representing a single lipid species, Fig. 4G in yellow, it is possible to highlight the tumor tissue, with cellular resolution.

Analysis of samples with a larger proportion of tumor shows interesting results. ccRCC tumors are particularly rich in lipids. Actually, the concentration of some lipid species is strikingly elevated in tumor [40]. In a previous paper, Jiráško et al. [41] already reported the existence of a higher abundance of glycosylated lipid species in ccRCC, mostly sulfoglycosphingolipids (sulfohexoxyl$_2$ ceramides, SHex$_2$Cer, according to the nomenclature used by the authors) and pointed to several species as possible candidates for biomarkers of ccRCC. As demonstrated in previous publications [42], these lipids play very specialized roles, related with regulation of urinary pH. Depending on the kidney area, cortex, medulla or papillae, the SHex$_2$Cer species presented differences in acyl

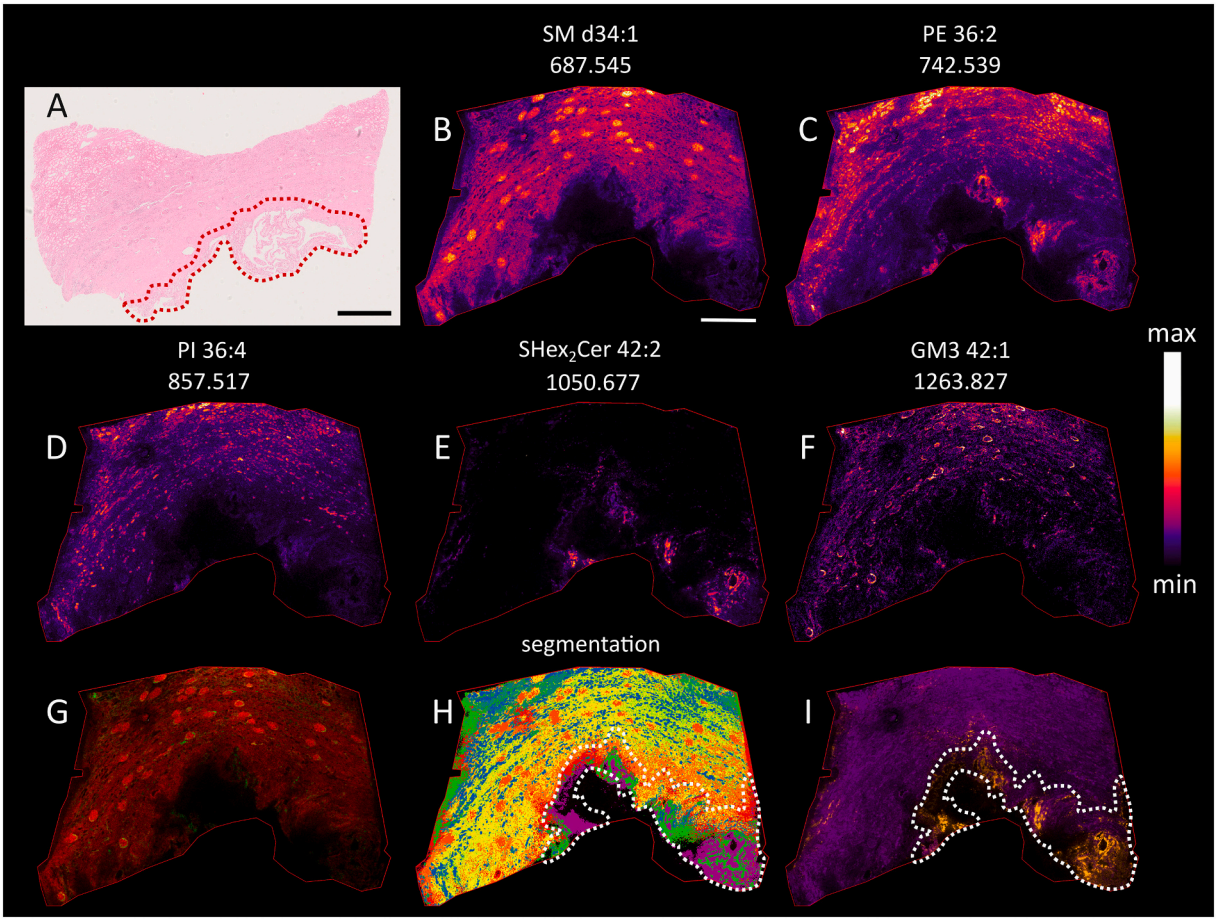

Fig. 4. A) H&E optical image of a paraffin section of human kidney containing a low grade (G1) ccRCC of solid-cystic structure. The red dotted line delimits the tumor; Distribution in a serial section of: B) SM d34:1, which is more abundant in glomeruli; C) PC 36:4, which is more abundant in PT I; D) PI 36:4, which is more abundant in CDT; E) SHex$_2$Cer 42:2, which is more abundant in tumor cells; F) GM3 42:1, which is more abundant in Bowman's capsule; G) Combination of SM d34.1 (red) and GM3 42:1 (green); H) supervised segmentation image: two populations of tumor cells were found (green and purple), encircled with a dashed line; G) all tumor cells exhibit a larger abundance of SHex$_2$Cer 42:2 (gold) than the rest of the tissue (purple). Experiment recorded in negative-ion mode with 10 μm/pixel. Scale bar 1 mm. (For interpretation of the references to color in this figure legend, the reader is referred to the web version of this article.)

composition and/or degree of hydroxylation [43], but the spatial resolution achieved in those studies did not enable a fine identification of the histological structures where each species was more abundant.

Fig. 5 shows the distribution of the $SHex_2Cer$ species detected in a section of human kidney containing the tumor-non tumor tissue transition. Assignment of the species in the figure was done following those in ref. [41]. In good agreement with previous publications [41–43], the $SHex_2Cer$ species present differential distributions, depending on their acyl composition or on the degree of hydroxylation.

The healthy tissue of the section in Fig. 5 (right side of the tissue) is mostly composed of glomeruli, PT I, PT II and CDT. A fibrotic barrier separates the uninvolved tissue areas from the tumor (lower-left part of the tissue), which presents a from a lipid composition point of view. Most species are present in PT I, PT II and tumor (see also Fig. 6), but the hydroxylated species are only found in PT II. Interestingly, such lipids present a very low abundance in tumor, as previously reported [44]. Conversely, those species present in PT I are also present in tumor, some of them with an increased abundance, such as $SHex_2Cer$ 40:0, 40:1,

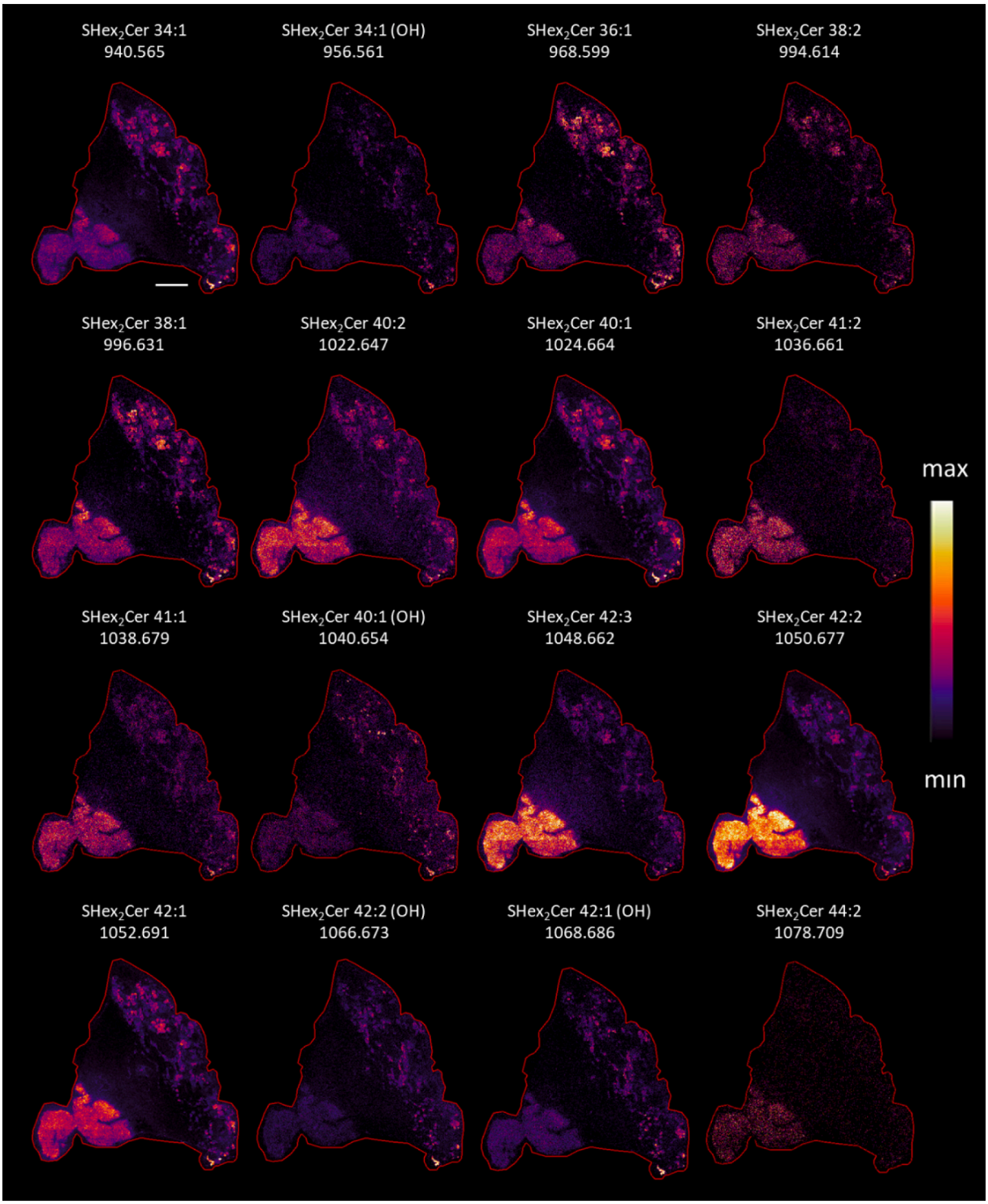

Fig. 5. Distribution of $SHex_2Cer$ species in a section of human kidney containing ccRCC. See text and the H&E staining in Fig. 6 for a histologic description of the tissue. Experiment carried out in negative polarity with 10 μm/pixel. Scale bar 1 mm.

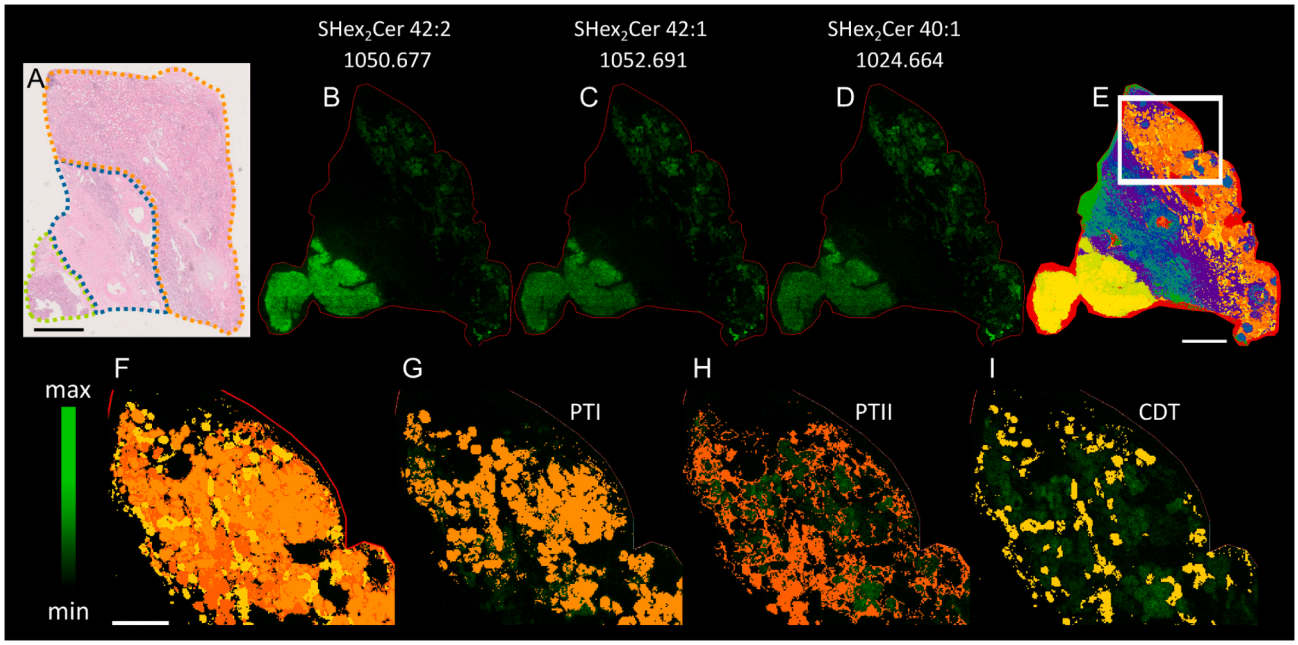

Fig. 6. A) H&E optical image of a paraffin section of a solid growth pattern ccRCC, composed of low-grade eosinophilic cells (G2), and surrounding non-tumor human kidney tissue. The tumor is surrounded by a dashed green line, the capsule by a blue line and the uninvolved tissue by an orange dashed line; (B)–(D) distribution(green scale) in a serial section of $SHex_2Cer$ 42:2, $SHex_2Cer$ 42:1 and $SHex_2Cer$40:1 respectively, which are more abundant in tumor but also present in healthy tissue; (E) Segmentation image. Based on their respective lipid fingerprint it was possible to identify segments delineating the glomeruli, PT I, PT II, CDT, the capsule of the tumor and several regions of the tumor itself. (F) Zoom over the area in the square in panel (E); (G)–(I) overlay of the PT I, PT II and CDT segments and the distribution of $SHex_2Cer$ 42:2 in green scale. Clearly, this lipid species is almost exclusively found in PT I, with a smaller abundance in PT II. Experiment performed in negative polarity with a 10 μm/pixel. Scale bar 1 mm. (For interpretation of the references to color in this figure legend, the reader is referred to the web version of this article.)

42:1, 42:2 and 42:3. Jirásko et al. [41] also reported the existence of a high abundance of $SHex_2Cer$ 40:1, 42:1 and 42:2 in ccRCC and identified them as possible candidates for biomarkers of ccRCC. The authors did not detect such species in healthy tissue, though. The detection of those species in this work raises a word of caution regarding the validity of $SHex_2Cer$ species as tumor biomarkers, but they may still serve to identify the origin of the tumor.

As described above, the PT I segment is located in the renal cortex and corresponds well with the description of the convoluted part of the proximal tubule by classical histology [45]. Single-cell RNA-sequencing studies have demonstrated that the cells of this segment of the proximal nephron share common transcriptional characteristics with ccRCC [46,47]. The presence of common genetic traces and more abundant lipid species such as $SHex_2Cer$ 36:1, 38:1, 40:1, 42:1, 42:2 and 42:3 add further evidence to the theory about the origin of ccRCC [31,32], and even points to a specific segment of the proximal tubule: its convoluted part [46,47].

The similarity of lipid signatures between PT I and tumor is interesting by itself: the tumor transformation did not silence the metabolic machinery required by the cell to produce these lipids. Conversely, their relative abundance is increased in tumor cells, indicate the existence of an evolutionary advantage. Certainly, previous studies pointed to an overexpression of GAL3ST1 (galactose-3-O-sulfotransferase 1, or CST) in ccRCC [48]. This enzyme catalyzes the transfer of a sulfate moiety from 3′-phosphoadenosine-5′-phosphosulfate (PAPS) to the lactose (or to the galactose in case of HexCer), as a final step in the synthesis of SHexCer and $SHex_2Cer$. Robinson et al. [49] demonstrated that *GAL3ST1* is a novel HIF-mediated gene that can be upregulated by both HIF1α and HIF2α, as a consequence of VHL loss or hypoxia. The expression of this gene was associated to poor outcome of ccRCC patients. They also showed that GAL3ST1 regulates sulfatide levels and demonstrated that the increase of GAL3ST1 in cancer cells facilitates the binding to platelets [49], which is a recognized mechanism to evade the action of the immune system and disseminate to distant organs [50].

Although further studies are required to clarify the involvement of these sulfatides in renal carcinogenetic processes, what is clear so far is the increasing abundance of selective $SHex_2Cer$ species in ccRCC tumors. These findings raise several additional questions. If the tumor cells preserve their original metabolic machinery to produce a variety of $SHex_2Cer$ species, one may expect that other RCC variants would present a differential lipid profile and therefore, LIMS experiments may become a powerful tool to help in the diagnosis of kidney tumors. Furthermore, it would be interesting to investigate if the same lipid profile is maintained in ccRCC metastasis.

4. Lipid signature and tumor heterogeneity

ccRCC is a paradigmatic example of intratumor heterogeneity (ITH) [51]. Subpopulations of tumor cells evolving over time interact differently with their microenvironment, leading some to acquire hallmarks that confer invasive properties and resistance to antitumor treatments. This phenomenon directly impacts patient prognosis and treatment response. The imaging methods and biomarkers available in pathology laboratories allow for limited classification of tumors and prognosis prediction. Over 30 % of ccRCCs initially diagnosed as non-advanced eventually relapse, indicating that the imaging tools currently available only scratch the surface of what is happening in this complex ecosystem [52,53].

Although they have not been adopted in clinical practice yet, the advent of multiplex image analysis techniques signifies a transformative era in pathological diagnosis and precision medicine for cancer treatment. Methods such as spatial trancriptomics [54,55] and multiplex IHC/IF [56] allow for the simultaneous and detailed assessment of multiple genomic and proteomic biomarkers, offering researchers a comprehensive understanding of spatial interactions within the ccRCC ecosystem. LIMS is a complementary method that permits observing

ccRCC and its ITH from the perspective of lipids [39].

For the future use of LIMS in clinical routine, the initial steps should be directed towards its combination with standard methods, such as H&E staining and IHC/IF, in the same or in consecutive tissue sections. As an example, Fig. 7 shows images of H&E staining, the segmentation analysis of LIMS, and IF of ccRCC tissues. In the first case (Fig. 7A–E), the segmentation analysis by LIMS clearly distinguishes the lipid fingerprint of the tumor (blue-purple), the stromal capsule (yellow-orange), and the adjacent non-tumor tissue in red. Alpha Smooth Muscle Actin (α-SMA) staining of stromal fibroblasts highlights the tumor capsule (Fig. 7D, in red), which is also visible with H&E (Fig. 7A) and has its own lipid fingerprint and correlates with the yellow-orange areas of the LIMS image (Fig. 7B). In the second ccRCC case (Fig. 7F–N), which is also described in Fig. 4, a double staining of CD31 and carbonic anhydrase 9 (CA9) was performed in the same section scanned by LIMS, to stain endothelial and tumor cells, respectively, in the tumor area. Both biomarkers are highly expressed in ccRCC tissue (Fig. 7H–J and L–N).

In addition to the areas well described in the H&E and IF images, LIMS also identifies tumor areas not distinguished by the other two techniques. For example, in Fig. 7B, parts of the capsule in close contact with tumor cells exhibit a distinct lipid fingerprint (yellow). Considering that fibroblasts are the main component of the tumor stroma [57], and that alterations in CAF lipid metabolism promote tumor growth [58], the presence of distinct lipid fingerprint areas within the capsule may be related to changes in the lipidome of these stromal cells based on their proximity to tumor cells. There are also internal tumor areas with different lipid profiles (green and purple areas) that point to the existence of tumor subpopulations with different metabolic profiles that H&E (Fig. 7A) do not distinguish.

In a previous study [39], we demonstrated that necrotic tissue in ccRCC also presents a well-defined lipid fingerprint. Indeed, tumors are usually composed of several cell populations with a variety of phenotypes, contending for resources and intermixed with necrotic and hypoxic areas. Necrosis is a poor prognostic indicator in ccRCC [31] and is identifiable by H&E. However, in that study, LIMS also detected that the periphery of necrotic tissue also presents a different lipid fingerprint. This suggests the presence of metabolic differences that H&E cannot detect and which may have biological and clinical relevance in a tumor characterized by neoangiogenic processes.

Fig. 8 shows a ccRCC with an eosinophilic phenotype, identifiable in the H&E staining (Fig. 8A), and associated with a poorer prognosis [31]. Again, what appears in the H&E image as a single population of eosinophilic cells (Fig. 8A and B) is divided in the LIMS image into at least two subpopulations of tumor cells with different fingerprints (Fig. 8C, green and red areas). The existence of different sub-populations of tumor cells is more clearly evidenced in the segmentation image, where, in addition, a clear distinction between the tumor areas, the capsule and the small portion of non-tumor tissue in the lower-right corner appear in different colors. The ability of LIMS to reveal the presence of distinct tumor cell populations could form the basis for its use as a diagnostic tool. Identifying cell populations with varying proliferative capacities or resistance to specific treatments may lead to improved diagnoses and more

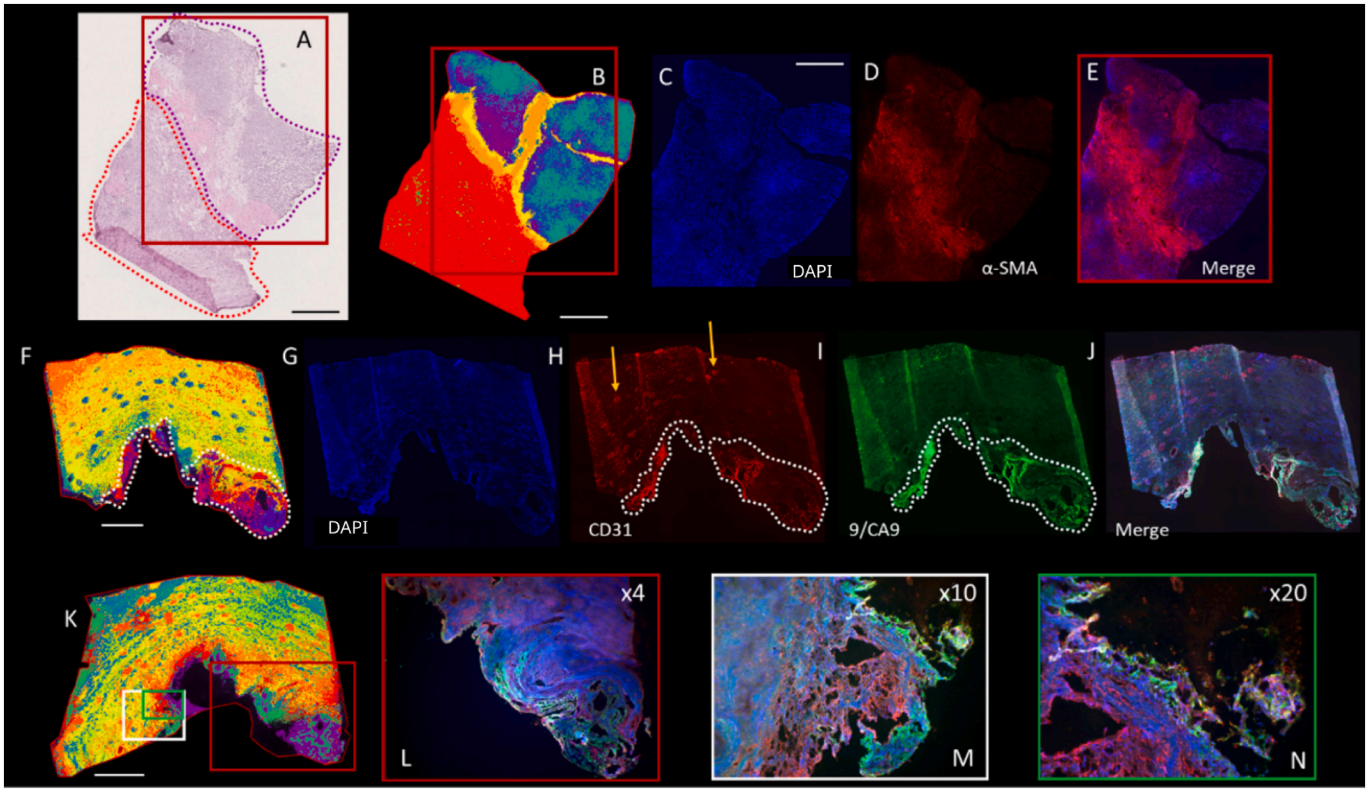

Fig. 7. Combination of LIMS and immunofluorescence (IF) in ccRCC tissue sections. A) H&E optical image of a fresh section of a low grade (G2) ccRCC with a nest growth in cords. The purple dotted line surrounds the tumor and capsule and the red one surrounds the uninvolved adjacent kidney tissue. The red box in this panel and in the next one marks the area shown in panels (C)—(E). B) Segmentation image of the LIMS experiment carried out over a consecutive section; (C)–(E) IF images of DAPI and α-SMA, and the overlay carried out on the same section scanned by LIMS. α-SMA is significantly expressed in the capsule surrounding tumor. (F) Segmentation image of the LIMS experiment performed over a human kidney section containing a ccRCC (the same case of Fig. 4); (G)–(J) IF images of DAPI, CD31, Carbonic Anhydrase 9 (CA9) and the overlay of both biomarkers. IF was carried out on the same section scanned by LIMS (see workflow on Fig. 1). CD31 is expressed in vessels (red) from tumor area (surrounded by dotted lines) but also in glomeruli (yellow arrows) from the uninvolved surrounding kidney tissue. CA9 is expressed in tumor cells (green) (K) Segmentation image of the LIMS experiment of a consecutive section (also shown in Fig. 4F); (L)–(N) Overlay of IF images of CD31 and CA9 on the tumor area of the same section scanned by LIMS. Scale bar 1 mm. (For interpretation of the references to color in this figure legend, the reader is referred to the web version of this article.)

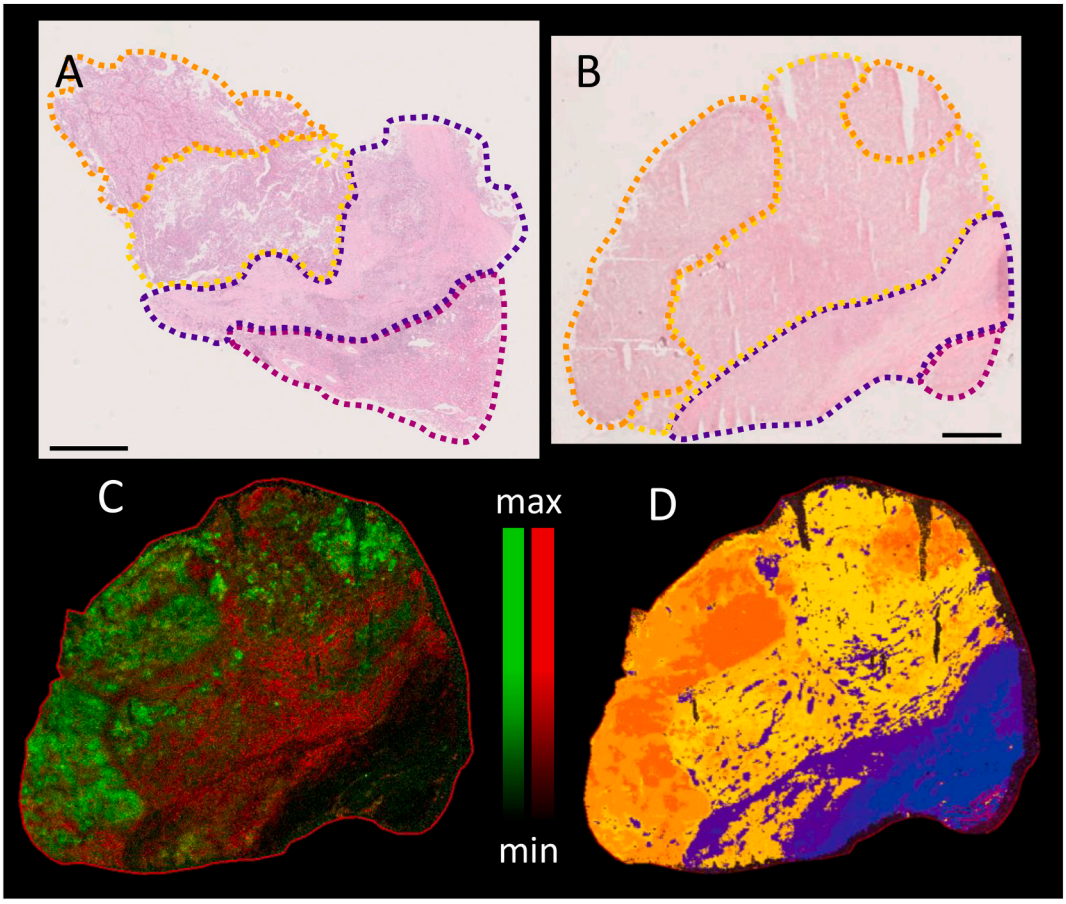

Fig. 8. A) H&E image of a paraffin section of a solid growth pattern ccRCC, composed of high-grade eosinophilic cells (G3) human kidney tissue. The area surrounded by the orange line contains ccRCC eosinophil variant tumor cells; the area surrounded by the yellow line corresponds to not-well preserved ccRCC tissue. The tumor capsule is surrounded in blue, while the purple area corresponds to non-tumor tissue. The color patter follows the LIMS segmentation image in panel (D); B) H&E image of a fresh-frozen section of the same tumor, measured by LIMS; C) Distribution of $SHex_2Cer$ 42:2 (1050.677, green) and m/z = 1235.807 (unassigned, red), highlighting two different tumor population cells; D) segmentation image of the LIMS experiment. Experiment carried out in negative-ion mode at 10 μm/pixel. Scale bar 1 mm. (For interpretation of the references to color in this figure legend, the reader is referred to the web version of this article.)

targeted therapies.

5. Concluding remarks

LIMS has an enormous potential to become a new kind of molecular histology that may open a new era in the diagnosis units of the hospitals. The examples shown here, demonstrate the potential of LIMS to reveal characteristics and histology areas on tissue sections that the standard imaging methods do not see. LIMS identifies the lipid phenotype of ITH, characteristic of many malignant tumors. Tumor areas easily identified with H&E (such as necrosis, eosinophilia, histological grade, etc.) have characteristic lipid fingerprints, because different histologic phenotypes are readily translated into different lipid fingerprints. Or in other words, there is an indissoluble connection between histologic phenotype and lipid fingerprint. Analyzing the tumor ecosystem with immunohistochemical biomarkers enables the detection of areas with subpopulations of tumor cells, immune cells, CAFs and endothelial cells. LIMS not only identifies such subpopulations but also some others that the "traditional" methodologies do not, as seen in the above examples. However, its application in clinics still requires of the measure of a massive number of samples and of the validation with orthogonal techniques. Luckily, LIMS is soft enough to enable performing several additional experiments over the same sample, facilitating the extraction of multimodal information. On the good side, it is possible to build libraries with the identified lipid fingerprints, associated to cell populations/phenotypes, as the fingerprints are preserved among individuals. Creating a detailed library of curated lipid fingerprints is the first step for the application of LIMS in clinics as a useful diagnosis tool.

The incorporation of new digital molecular histopathology methods, such as spatial transcriptomics or multiplex IHC, in combination with LIMS, illuminates a horizon of significant changes in tissue imaging analysis and in the routine of pathology services of the hospitals. The simultaneous detection of thousands of transcripts, proteins and lipid species in a tumor section requires advanced software and AI algorithms to comprehend all the information. However, it has the potential to qualitatively improve tumor classification and the understanding of tumor biology, enabling the discovery of better prognostic and treatment response biomarkers, as well as identifying new molecular targets for this era of precision medicine we are entering in this century.

CRediT authorship contribution statement

Ibai Calvo: Writing – review & editing, Investigation, Formal analysis, Data curation. **Olatz Fresnedo:** Writing – review & editing, Methodology, Investigation, Formal analysis. **Lorena Mosteiro:** Writing – review & editing, Investigation, Data curation. **José I. López:** Writing – review & editing, Methodology, Investigation, Formal analysis, Data curation. **Gorka Larrinaga:** Writing – review & editing, Validation, Supervision, Resources, Project administration, Methodology, Investigation, Funding acquisition, Data curation, Conceptualization. **José A. Fernández:** Writing – review & editing, Writing – original draft, Visualization, Validation, Supervision, Resources, Project administration,

Methodology, Funding acquisition, Conceptualization.

Declaration of competing interest

The authors declare that they have no known competing financial interests or personal relationships that could have appeared to influence the work reported in this paper.

Data availability

Data will be made available on request.

Acknowledgements

This project was supported by a grant from the Basque Government (grants IT1491-22 and KK-2024/00003). IC thanks the Basque Government for his predoctoral fellowship. The authors acknowledge the technical support and mass spectrometry resources provided by SGIker (UPV/EHU) as well as the microscope facilities provided by SGIker (UPV/EHU).

Appendix A. Supplementary data

Supplementary data to this article can be found online at https://doi.org/10.1016/j.bbalip.2024.159568.

References

[1] G. Liebisch, E. Fahy, J. Aoki, E.A. Dennis, T. Durand, C.S. Ejsing, et al., Update on LIPID MAPS classification, nomenclature, and shorthand notation for MS-derived lipid structures, J. Lipid Res. 61 (12) (2020) 1539–1555.
[2] S. Cockcroft, Mammalian lipids: structure, synthesis and function, Essays Biochem. 65 (5) (2021) 813–845.
[3] E. Muro, G.E. Atilla-Gokcumen, U.S. Eggert, Lipids in cell biology: how can we understand them better? Mol. Biol. Cell 25 (12) (2014 Jun 15) 1819–1823.
[4] A.L. Santos, G. Preta, Lipids in the cell: organisation regulates function, Cell. Mol. Life Sci. 75 (11) (2018) 1909–1927.
[5] B. Kadereit, P. Kumar, W. Wang, D. Miranda, E.L. Snapp, N. Severina, et al., Evolutionarily conserved gene family important for fat storage, Proc. Natl. Acad. Sci. U. S. A. 105 (1) (2008 Jan 8) 94–99.
[6] G.E. Janssens, M. Molenaars, K. Herzog, L. Grevendonk, C.M.E. Remie, M.A. T. Vervaart, et al., A conserved complex lipid signature marks human muscle aging and responds to short-term exercise, Nature Aging 4 (5) (2024) 681–693.
[7] Z. Wu, G.I. Bagarolo, S. Thoröe-Boveleth, J. Jankowski, "Lipidomics": mass spectrometric and chemometric analyses of lipids, Adv. Drug Deliv. Rev. 159 (2020) 294–307.
[8] D. Smirnov, P. Mazin, M. Osetrova, E. Stekolshchikova, E. Khrameeva, The hitchhiker's guide to untargeted lipidomics analysis: practical guidelines, Metabolites 11 (11) (2021 Oct 20) 713, https://doi.org/10.3390/metabo11110713.
[9] F. Hillenkamp, M. Karas, R.C. Beavis, B.T. Chait, Matrix-assisted laser desorption/ionization mass spectrometry of biopolymers, Anal. Chem. 63 (24) (1991) 1193A–1203A.
[10] K. Tanaka, H. Waki, Y. Ido, S. Akita, Y. Yoshida, T. Yoshida, et al., Protein and polymer analyses up to m/z 100 000 by laser ionization time-of-flight mass spectrometry, Rapid Commun. Mass Spectrom. 2 (8) (1988) 151–153.
[11] M. Karas, F. Hillenkamp, Laser desorption ionization of proteins with molecular masses exceeding 10,000 daltons, Anal. Chem. 60 (20) (1988) 2299–2301.
[12] R.M. Caprioli, T.B. Farmer, H.Y. Zhang, M. Stoeckli, Molecular imaging of biological samples by MALDI MS, Abstr. Pap. Am. Chem. Soc. 214 (1997), 113-ANYL.
[13] M. Stoeckli, T.B. Farmer, R.M. Caprioli, Automated mass spectrometry imaging with a matrix-assisted laser desorption ionization time-of-flight instrument, J. Am. Soc. Mass Spectrom. 10 (1) (1999) 67–71.
[14] M. Kompauer, S. Heiles, B. Spengler, Atmospheric pressure MALDI mass spectrometry imaging of tissues and cells at 1.4-μm lateral resolution, Nat. Methods 14 (1) (2017) 90–96.
[15] J.M. Wiseman, D.R. Ifa, Q. Song, R.G. Cooks, Tissue imaging at atmospheric pressure using desorption electrospray ionization (DESI) mass spectrometry, Angew. Chem. Int. Ed. 45 (43) (2006) 7188–7192.
[16] P. Nemes, A.A. Barton, Y. Li, A. Vertes, Ambient molecular imaging and depth profiling of live tissue by infrared laser ablation electrospray ionization mass spectrometry, Anal. Chem. 80 (12) (2008) 4575–4582.
[17] L. Martín-Saiz, L. Mosteiro, J. Solano-Iturri, Y. Rueda, J. Martín-Allende, I. Imaz, et al., High-resolution human kidney molecular histology by imaging mass spectrometry of lipids, Anal. Chem. 93 (27) (2021) 9364–9372.
[18] E.A. Jones, S. Deininger, P.C.W. Hogendoorn, A.M. Deelder, L.A. McDonnell, Imaging mass spectrometry statistical analysis, J. Proteomics 75 (16) (2012) 4962–4989.
[19] T. Alexandrov, MALDI imaging mass spectrometry: statistical data analysis and current computational challenges, BMC Bioinform. 13 (2012) S11.
[20] G. Xu, S. Gan, B. Guo, L. Yang, Application of clustering strategy for automatic segmentation of tissue regions in mass spectrometry imaging, Rapid Commun. Mass Spectrom. 38 (8) (2024) e9717.
[21] M. Tuck, F. Grélard, L. Blanc, N. Desbenoit, MALDI-MSI towards multimodal imaging: challenges and perspectives, Front. Chem. (2022) 10.
[22] T. Porta Siegel, G. Hamm, J. Bunch, J. Cappell, J.S. Fletcher, K. Schwamborn, Mass spectrometry imaging and integration with other imaging modalities for greater molecular understanding of biological tissues, Mol. Imaging Biol. 20 (6) (2018) 888–901.
[23] M. Aichler, A. Walch, MALDI imaging mass spectrometry: current frontiers and perspectives in pathology research and practice, Lab. Invest. 95 (4) (2015) 422–431.
[24] A. Rompp, S. Guenther, Y. Schober, O. Schulz, Z. Takats, W. Kummer, et al., Histology by mass spectrometry: label-free tissue characterization obtained from high-accuracy bioanalytical imaging, Angew. Chem. Int. Ed. 49 (22) (2010) 3834–3838.
[25] D. Touboul, O. Laprévote, A. Brunelle, Micrometric molecular histology of lipids by mass spectrometry imaging, Curr. Opin. Chem. Biol. 15 (5) (2011) 725–732.
[26] K. Mallah, K. Zibara, C. Kerbaj, A. Eid, N. Khoshman, Z. Ousseily, et al., Neurotrauma investigation through spatial omics guided by mass spectrometry imaging: target identification and clinical applications, Mass Spec. Rev. 42 (1) (2023) 189–205.
[27] M.S. Bergholt, A. Serio, J.S. McKenzie, A. Boyd, R.F. Soares, J. Tillner, et al., Correlated heterospectral lipidomics for biomolecular profiling of remyelination in multiple sclerosis, ACS Cent. Sci. 4 (1) (2018) 39–51.
[28] A.B. Esselman, N.H. Patterson, L.G. Migas, M. Dufresne, K.V. Djambazova, M. E. Colley, et al., Microscopy-directed imaging mass spectrometry for rapid high spatial resolution molecular imaging of glomeruli, J. Am. Soc. Mass Spectrom. 34 (7) (2023) 1305–1314.
[29] H. Moch, M.B. Amin, D.M. Berney, E.M. Compérat, A.J. Gill, A. Hartmann, et al., The 2022 World Health Organization classification of tumours of the urinary system and male genital organs—part a: renal, penile, and testicular tumours, Eur. Urol. 82 (5) (2022) 458–468.
[30] R. Elias, Q. Zhang, J. Brugarolas, The von Hippel-Lindau tumor suppressor gene: implications and therapeutic opportunities, Cancer J. 26 (5) (2020) 390–398.
[31] G.T. MacLennan, L. Cheng, 2 - neoplasms of the kidney, in: Urologic Surgical Pathology (Fourth Edition) 83, 2020, 163.e23.
[32] A.M. Raghubar, M.J. Roberts, S. Wood, H.G. Healy, A.J. Kassianos, A.J. Mallett, Cellular milieu in clear cell renal cell carcinoma, Front. Oncol. (2022) 12.
[33] Y. Gu, S. Cohn, A. Christie, T. McKenzie, N. Wolff, Q.N. Do, et al., Modeling renal cell carcinoma in mice: Bap1 and Pbrm1 inactivation drive tumor grade, Cancer Discov. 7 (8) (2017) 900–917.
[34] A. Madrazo-Ibarra, P. Vaitla, Histology, Nephron, StatPearls Publishing LLC, StatPearlsTreasure Island (FL), 2022.
[35] N. Verbeeck, R.M. Caprioli, R. Van de Plas, Unsupervised machine learning for exploratory data analysis in imaging mass spectrometry, Mass Spec. Rev. 39 (3) (2020) 245–291.
[36] N. Verbeeck, J. Yang, B. De Moor, R.M. Caprioli, E. Waelkens, Van dP., Automated anatomical interpretation of ion distributions in tissue: linking imaging mass spectrometry to curated atlases, Anal. Chem. 86 (18) (2014) 8974–8982.
[37] D.P. Van, K. Pelckmans, B. De Moor, E. Waelkens, Spatial querying of imaging mass spectrometry data: a nonnegative least squares approach, in: NIPS workshop on Machine Learning in Computational Biology 2007, Whistler, Canada, 2007, pp. 1–4.
[38] F. Ojeda, M. Signoretto, Waelkens E. Van DP, B.D. Moor, J. Suykens, Semi-supervised learning of sparse linear models in mass spectral imaging, in: Lecture Notes in Bioinformatics 6282, 2010, pp. 325–334.
[39] L. Martín-Saiz, B. Abad-García, J. Solano-Iturri, L. Mosteiro, J. Martín-Allende, Y. Rueda, et al., Using the synergy between HPLC-MS and MALDI-MS imaging to explore the lipidomics of clear cell renal cell carcinoma, Anal. Chem. 95 (4) (2023) 2285–2293.
[40] K. Saito, E. Arai, K. Maekawa, M. Ishikawa, H. Fujimoto, R. Taguchi, et al., Lipidomic signatures and associated transcriptomic profiles of clear cell renal cell carcinoma, Sci. Rep. 30 (6) (2016 Jun) 28932.
[41] R. Jirásko, M. Holčapek, M. Khalikova, D. Vrána, V. Študent, Z. Prouzová, et al., MALDI orbitrap mass spectrometry profiling of dysregulated sulfoglycosphingolipids in renal cell carcinoma tissues, J. Am. Soc. Mass Spectrom. 28 (8) (2017) 1562–1574.
[42] C. Marsching, M. Rabionet, D. Mathow, R. Jennemann, C. Kremser, S. Porubsky, et al., Renal sulfatides: sphingoid base-dependent localization and region-specific compensation of CerS2-dysfunction1[S], J. Lipid Res. 55 (11) (2014) 2354–2369.
[43] C. Marsching, R. Jennemann, R. Heilig, H. Gröne, C. Hopf, R. Sandhoff, Quantitative imaging mass spectrometry of renal sulfatides: validation by classical mass spectrometric methods1[S], J. Lipid Res. 55 (11) (2014) 2343–2353.
[44] I.C. Kim, G. Bang, J.H. Lee, K.P. Kim, Y.H. Kim, H.K. Kim, et al., Low C24-OH and C22-OH sulfatides in human renal cell carcinoma, J. Mass Spectrom. 49 (5) (2014 May) 409–416.
[45] A standard nomenclature for structures of the kidney. The Renal Commission of the International Union of Physiological Sciences (IUPS), Am. J. Physiol. 254(1 Pt 2):1 (1988 Jan).

[46] M.D. Young, T.J. Mitchell, F.A. Vieira Braga, M.G.B. Tran, B.J. Stewart, J. R. Ferdinand, et al., Single-cell transcriptomes from human kidneys reveal the cellular identity of renal tumors, Science 361 (6402) (2018 Aug 10) 594–599.
[47] Y. Zhang, S.P. Narayanan, R. Mannan, G. Raskind, X. Wang, P. Vats, et al., Single-cell analyses of renal cell cancers reveal insights into tumor microenvironment, cell of origin, and therapy response, Proc. Natl. Acad. Sci. U. S. A. 118 (24) (2021 Jun 15) e2103240118, https://doi.org/10.1073/pnas.2103240118.
[48] S. Porubsky, M. Nientiedt, M.C. Kriegmair, J.H. Siemoneit, R. Sandhoff, R. Jennemann, et al., The prognostic value of galactosylceramide-sulfotransferase (Gal3ST1) in human renal cell carcinoma, Sci. Rep. 11 (1) (2021 May 25) 10926.
[49] C.M. Robinson, B.P.K. Poon, Y. Kano, F.G. Pluthero, W.H.A. Kahr, M. Ohh, A hypoxia-inducible HIF1-GAL3ST1-sulfatide axis enhances ccRCC immune evasion via increased tumor cell-platelet binding, Mol. Cancer Res. 17 (11) (2019 Nov) 2306–2317.
[50] M. Haemmerle, R.L. Stone, D.G. Menter, V. Afshar-Kharghan, A.K. Sood, The platelet lifeline to cancer: challenges and opportunities, Cancer Cell 33 (6) (2018 Jun 11) 965–983.
[51] Z. Tippu, L. Au, S. Turajlic, Evolution of renal cell carcinoma, Eur. Urol. Focus 7 (1) (2021) 148–151.
[52] J. Deng, S. Tu, L. Li, G. Li, Y. Zhang, Diagnostic, predictive and prognostic molecular biomarkers in clear cell renal cell carcinoma: a retrospective study, Cancer Reports 7 (6) (2024) e2116.
[53] F. Sanguedolce, R. Mazzucchelli, U.G. Falagario, A. Cormio, M. Zanelli, A. Palicelli, et al., Diagnostic biomarkers in renal cell tumors according to the latest WHO classification: a focus on selected new entities, Cancers (Basel) 16 (10) (2024 May 13) 1856, https://doi.org/10.3390/cancers16101856.
[54] M. Cheng, Y. Jiang, J. Xu, A.A. Mentis, S. Wang, H. Zheng, et al., Spatially resolved transcriptomics: a comprehensive review of their technological advances, applications, and challenges, J. Genet. Genomics 50 (9) (2023) 625–640.
[55] J. Hu, S. Wang, Y. Hou, Z. Chen, L. Liu, R. Li, et al., Multi-omic profiling of clear cell renal cell carcinoma identifies metabolic reprogramming associated with disease progression, Nat. Genet. 56 (3) (2024) 442–457.
[56] N.H. Chakiryan, Y. Kim, A. Berglund, A. Chang, G.J. Kimmel, A. Hajiran, et al., Geospatial characterization of immune cell distributions and dynamics across the microenvironment in clear cell renal cell carcinoma, J. Immunother. Cancer 11 (4) (2023 Apr) e006195, https://doi.org/10.1136/jitc-006195.
[57] A. Peltier, R. Seban, I. Buvat, F. Bidard, F. Mechta-Grigoriou, Fibroblast heterogeneity in solid tumors: from single cell analysis to whole-body imaging, Semin. Cancer Biol. 86 (2022) 262–272.
[58] S. Peng, Y. Li, M. Huang, G. Tang, Y. Xie, D. Chen, et al., Metabolomics reveals that CAF-derived lipids promote colorectal cancer peritoneal metastasis by enhancing membrane fluidity, Int. J. Biol. Sci. 18 (5) (2022 Feb 21) 1912–1932.